Received: 5 July 2023 | Revised: 28 August 2023 | Accepted: 2 September 2023

IET Electric Power Applications

DOI: 10.1049/elp2.12366

ORIGINAL RESEARCH

Design and analysis of PM-assisted synchronous reluctance machine with shifted magnetic poles

Seyyed Morteza Mousavi Bafrouei[1] | **Aliakbar Damaki Aliabad**[1] | **Ebrahim Amiri**[2]

[1]Electrical Engineering Department, Yazd University, Yazd, Iran

[2]Electrical Engineering Department, California State University-Long Beach, Long Beach, California, USA

Correspondence
Aliakbar Damaki Aliabad.
Email: alidamaki@yazd.ac.ir

Abstract

The authors present a new design of a PM-assisted synchronous reluctance motor (PM-SynRM) with uneven air-gap length to improve the power factor and enhance the torque production capability. The rotor structure is modified to properly shift rotor magnetic poles and therefore (i) increases the back-EMF and the electromagnetic torque, (ii) allows electromagnetic torque and reluctance torque components peak near the same current phase angle. The proposed solution is simple, does not require changing the arrangement of magnets and/or flux barriers and is applicable to all types of PM-SynRMs. Sensitivity analysis is carried out to determine the extent of which the proposed magnetic pole shifting may impact the resultant torque profile. To assess the level of success, the electromagnetic characteristics of the proposed design (e.g. torque, power factor, and back-EMF) are compared against the baseline structure under the same operating conditions. For verification purposes, Finite Element simulation results are validated via a series of analytical calculations and experimental measurements, and supported with detailed theoretical discussion.

KEYWORDS

permanent magnets, reluctance motors, torque

1 | INTRODUCTION

Research and development of synchronous reluctance machines (SynRM) are gaining popularity and have become a subject of interest among scholars and various industry sectors. Despite simple structure and low manufacturing cost, their industrial application is still limited because of their inherent low torque delivery and poor power factor. These issues could be addressed by incorporating a small amount of Permanent Magnet (PM) material to the machine structure, generally known as PM-Assisted SynRM. Thereby, the PM-Assisted classes are widely disseminated in various industrial application such as electric vehicles [1], water pumps [2], air conditioner compressors [3] etc.

The structure and the position of PMs should be properly adjusted to ensure that certain performance criteria are satisfied. For this purpose, various objective functions are defined (e.g. high torque density, low saturation risk etc), and formulated in single-objective or multi-objective optimisation algorithms [4–8]. In addition, to offset the high cost of rare-earth magnetic materials, attempts are made to replace a portion of high-energy rare-earth magnets with low energy ferrite magnets subject to a condition that the rated torque density of the machine is preserved [9, 10]. Despite recent advancements in research and development of PM-Assisted SynRMs, some design challenges and operational setbacks are yet to be addressed. In particular, the peak electromagnetic torque and reluctance torque components naturally occur when current phase angles are 45 electrical degrees apart, and therefore the electromagnetic torque may not be fully materialised at the output. In other words, the resultant torque delivery of the machine is always below the algebraic sum of the electromagnetic and reluctance torque components. Thereby, latest published research documents include proposals/solutions to minimising the angular displacement between the two torque components, and potentially increasing the PM contribution in the output power delivery. Examples include topologies with two-segmented rotor (IPM segment and SynRM segment) in ref. [11], and (SPM segment and SynRM segment) in ref. [12], where the rotor magnetic structure is arranged and designed independently from the reluctance structure. In other words, the rotor magnetic structure is not restricted to the limited space of the flux barriers. However, the construction is quite complex and requires larger stack length to accommodate the two rotor segments. In ref. [13], an asymmetrical rotor configuration is proposed to change the direction of magnetic flux and allow the electromagnetic and reluctance torque components peak near or at the same current phase angle. However, the presented asymmetrical rotor structure slightly weakens the reluctance property, which may partially nullify the gain obtained by aligning the torque components. In addition, due to specific structure of the flux barriers the rotor does not have sufficient mechanical strength. In ref. [14], the rotor is equipped with assisted barriers to allow the torque components peak around the same current phase angle, but the presented solution changes the saliency ratio of the rotor. In addition, the solution is exclusive to machine topologies with V-shape magnets and may not be generalised to all classes of PM-Assisted SynRMs. In ref. [15], the PMs are relocated toward the outer surface of the rotor to divert the d-axis of magnetic flux by about 45° electrical, but it creates an asymmetrical radial orientation of flux barriers. Deforming structural order of flux barriers could to some extent weaken the reluctance property of the machine. The aforementioned documents share the same goal of getting the full use of the electromagnetic torque, and the same objective of restructuring the rotor layout, but their implementation is different (i.e. either by re-arranging rotor magnets or by re-arranging rotor flux barriers). Although, presented solutions offer a new perspective in designing the next generation of PM-Assisted SynRMs, the research gap still exists as each design comes with a certain limitation(s) as described above.

Motivated by the significant potentials of PM-Assisted SynRMs, this paper aims to improve the electromagnetic performance of the machine by continuing and building upon the previous research efforts. In the proposed structure, the rotor flux/pole is shifted/diverted by a certain angle towards the q axis to synchronise the peak electromagnetic torque with the peak reluctance torque at or near a same load angle. For this purpose, the magnetic pole air gap is reduced in one side of the pole (strengthening rotor PM flux in one side) and proportionately increased on the other side (weakening rotor PM flux in the other side of the pole). This shifts the angle of the rotor flux, and thereby the rotor pole by a certain degree. In addition to aligning/synching the two torque components, this arrangement also increases the back-EMF and allows the machine to generate a higher electromagnetic torque. Unlike existing solutions, the arrangement of rotor magnets and rotor flux barriers are not altered. In addition, the proposed rotor structure is simple, does not weaken the reluctance property of the motor, and the rotor mechanical strength is preserved. Moreover, the proposed structure is not limited to a certain type and can be implemented across the board to all classes of PM-Assisted SynRMs. The paper is organised as follows. Section 2 discusses the proposed structure and its working theory. Section 3 presents the Finite Element (FE) simulated electromagnetic performance of the machine followed by experimental validation in Section 4, and concluding remarks in section 5.

2 | PROPOSED STRUCTURE AND OPERATIONAL THEORY

2.1 | Conventional/baseline structure

Figure 1 presents the schematic of the conventional structure, which also serves as the baseline machine for comparative analysis. The stator includes 24 slot with 4-pole, 3-phase distributed winding arrangement (Figure 1a). The rotor layout includes 4 magnetic and 4 reluctance pole numbers with 4 layers of flux barriers along the radial direction (Figure 1b). As seen, the size of the inner magnets (i.e. towards the rotor shaft) is relatively larger than the outer ones. This type of magnetic arrangement may improve the flux flow and avoid magnets demagnetisation as reported in ref. [16–18].

The relationship between various quantities such as current, voltage, and flux can be described by relations Equation (1), and the corresponding vector diagram in d-q reference frame is shown in Figure 2a. The resultant torque is the sum of the electromagnetic torque and reluctance torque components as expressed in Equation (2) [15]:

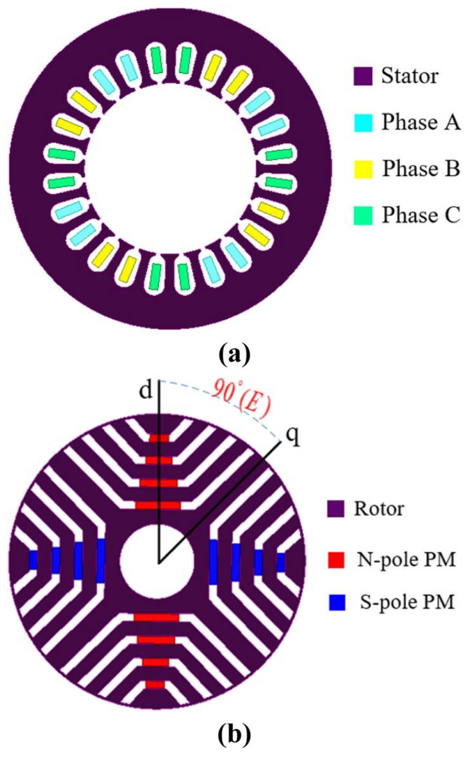

FIGURE 1 Conventional structure (a) Stator section and (b) rotor layout.

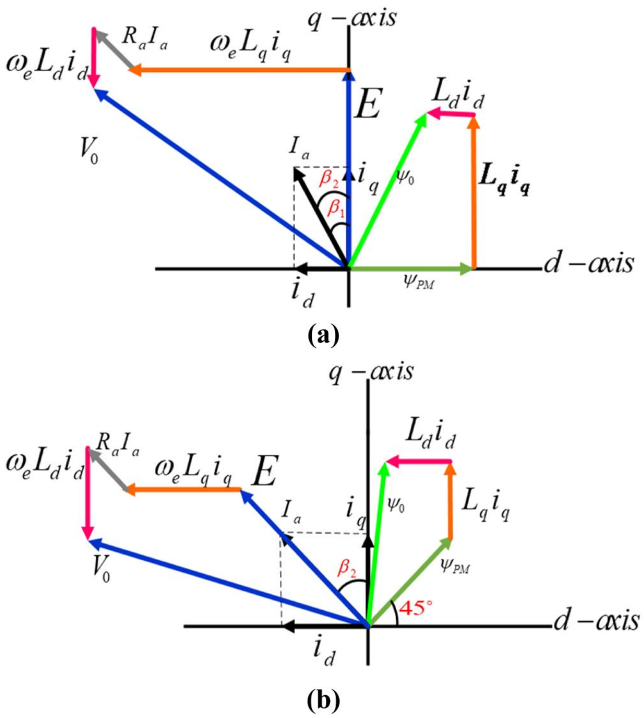

FIGURE 2 Vector diagram in d-q reference frame (a) conventional case, and (b) ideal case.

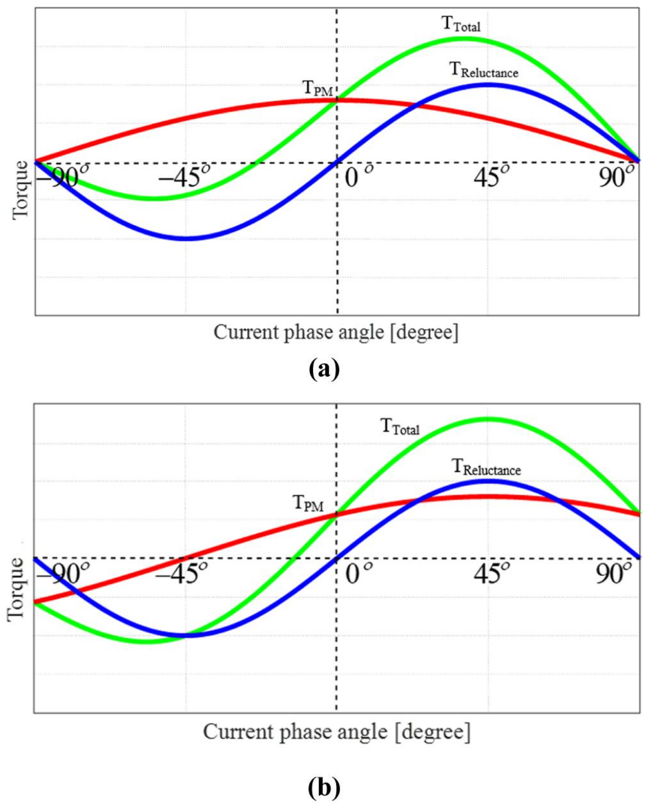

FIGURE 3 Torque characteristic versus current angle (a) conventional case and (b) ideal case.

$$V_o = E + R_a I_a + j\omega_e\left(L_q i_q + L_d i_d\right) \tag{1a}$$

$$I_a = \sqrt{{i_d}^2 + {i_q}^2} \tag{1b}$$

$$\psi_0 = \sqrt{\left(\psi_{\rm PM} - L_d i_d\right)^2 + \left(L_q i_q\right)^2} \tag{1c}$$

$$T_{\rm Total} = \frac{3P}{2}\left[\lambda_{\rm PM} I_a \cos\beta_1 + \frac{1}{2}\left(L_q - L_d\right) I_a^2 \sin 2\beta_2\right] \tag{2}$$

where p is the number of pole pairs, I_a is the maximum phase (i.e. phase *a*) current, β_1 is the angle between phase *a* stator current and the back-EMF (E), β_2 is the angle between phase *a* stator current and the q-axis, L_d and L_q represent inductance of the d-q axes, ω_e is the angular speed, $\Psi_{\rm PM}$ and Ψ_0 are magnet flux and resultant flux, respectively and $\lambda_{\rm pm}$ is the maximum flux linkage per phase.

As shown in Figure 2a, angles β_1 and β_2 are equal ($\beta_1 = \beta_2$) in the conventional structure. According to Equation (2), the reluctance torque oscillates as twice the higher frequency as the electromagnetic torque and peaks at $\beta_2 = \beta_1 =$ 45^o whilst the electromagnetic torque peaks at $\beta_1 = \beta_2 =$ 0^o. Therefore, the motor is typically driven at a current angle in between 0^o and 45^o (0$^o \ll \beta_2 = \beta_1 \ll$ 45^o). Figure 3a illustrates the corresponding torque profile versus current angle. It is evident the peak reluctance torque and electromagnetic torque components are 45^o apart, meaning the machine cannot simultaneously operate at maximum electromagnetic and maximum reluctance torque capacity.

2.2 | Ideal case

Ideally, it is desired that both the reluctance and electromagnetic torque components peak at the same current phase angle (as shown in a hypothetical drawing of Figure 3b), thus increasing maximum output torque delivery of the machine. The corresponding vector diagram of the ideal case is presented in Figure 2b, highlighting the angular shift of the rotor flux and the back-EMF vector. With this arrangement, the angle between stator current vector (I_a) and the back-EMF vector (E) falls to zero (β_1 = 0^o), while the angle between stator current vector (I_a) and the q-axis remains unchanged (β_2 = 45^o), as illustrated in the vector diagram of Figure 2b. According to Equation (2), the electromagnetic torque utility peaks at β_1 = 0^o, and the reluctance torque utility peaks at β_2 = 45^o. Since both criteria are fulfilled under a same current angle, the resultant torque can reach the maximum capacity.

2.3 | Proposed structure

To synchronise the peak electromagnetic torque with the peak reluctance torque near a same current angle, the rotor magnetic flux is diverted toward q-axis by a certain angle (ideally 45^o). For this purpose, the rotor core radii is extended by + 0.2 mm along half a magnetic pole arc angle, and is equally shorten by - 0.2 mm along the other half of the magnetic pole arc angle.

This forms a rotor structure with uneven air gap along the magnetic pole arc angle as shown in schematic of Figure 4a. For a better visibility, the circumferential area with uneven rotor radii (uneven air-gap) are zoomed-in. To further highlight the structural differences between the two machines, Figure 4b illustrates the rotor radii of the baseline structure versus the proposed structure along 180° circumferential angle. Given that the arrangement and the structure of flux barriers in both the proposed and the baseline structures are similar, the rotor retains its original mechanical stiffness. By the same token, the length of the airgap along q-axis remains the same. However, the saliency created by the uneven air-gap forms a relatively higher saliency ratio $\left(\frac{L_d}{L_q}\right)$ in the proposed structure. In other words, in addition to the saliency created by the rotor flux barriers (first source of saliency), the reduction and the extension of the airgap along the rotor circumference further increases the salient characteristic of the rotor. To better perceive this second source of saliency Figure 4c shows the rotor layout of the proposed structure without rotor flux barriers. Therefore, the reluctance torque of the proposed structure is expected to be slightly higher as confirmed by FE simulation results in the next section.

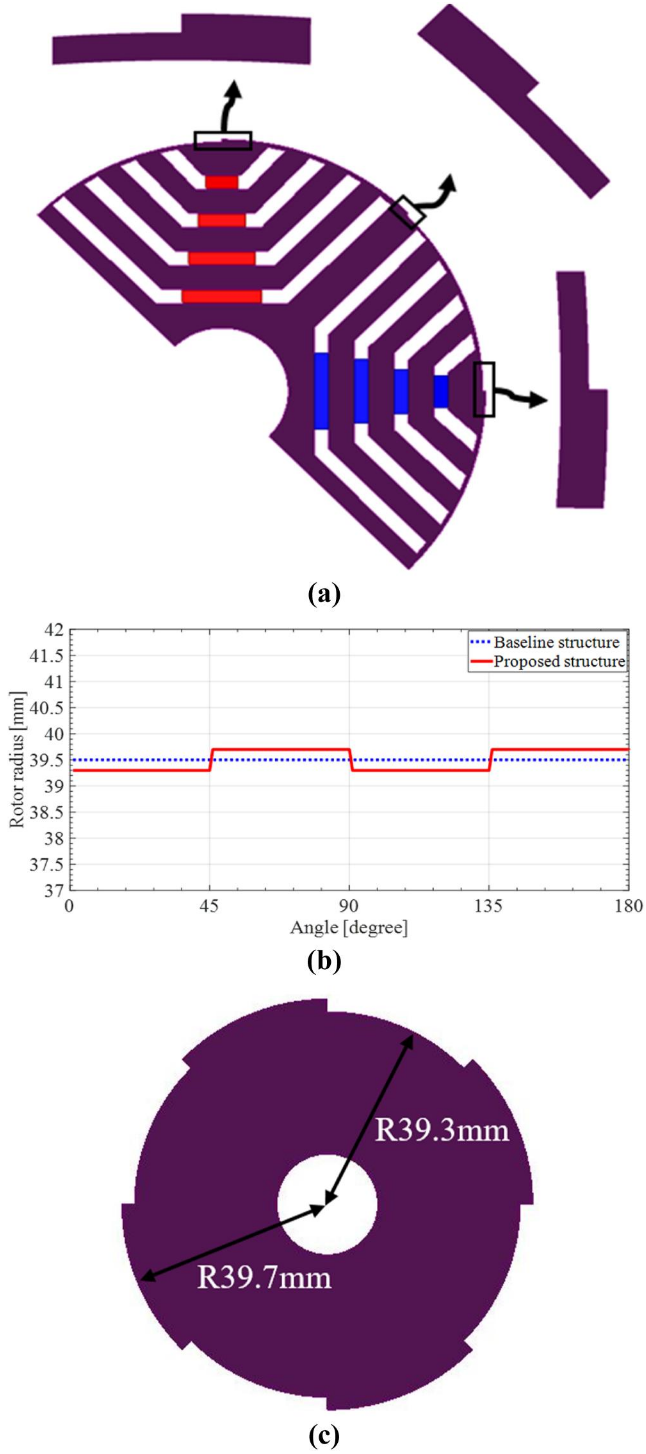

FIGURE 4 Proposed structure with uneven air gap along the magnetic pole (a) rotor layout, cross-sectional view (b) rotor radii along circumferential angle, and (c) rotor layout without flux barriers.

3 | RESULTS AND DISCUSSION

The proposed scheme is modelled in a FE software package and simulated at five different cases (within the range of ±10% to ± 50% of the airgap) to determine the sensitivity of the maximum torque delivery to the proposed solution. The data/specifications of the machine (e.g. machine size/dimension, winding arrangement, and rotor layout) are all identical to the conventional (baseline) machine, with the only exception being the length of the air gap as described in Section 2.2. Detailed specifications are listed in Table 1.

3.1 | PM flux distribution and Back-EMF

The no-load magnetic circuit model representing one pole of the proposed design (Figure 5a) is developed and shown in Figure 5b. In this model, PMs and saturated bridges are modelled with constant current sources (φ_{pm1}, φ_{pm2}, φ_{pm3}, φ_{pm4}, φ_{b1}, φ_{b2}, φ_{b3}, φ_{b4}), while flux barriers and air gap regions are modelled with reluctance elements (R_1, R_2, R_3, R_4). The values of current sources and reluctance elements are related to structural parameters of the machine and the PM remnant flux density. The derivation procedure of magnetic circuit parameters of a conventional IPM machine can be found in ref. [19, 20]. Using the source transformation Equation (3) the detailed magnetic circuit model shown in Figure 5b can be simplified as Figure 5c.

$$V_1 = R_1\left(\varphi_{pm1} - \varphi_{b1}\right) \tag{3a}$$

$$V_2 = R_2\left(\varphi_{pm2} - \varphi_{b2}\right) \tag{3b}$$

$$V_3 = R_3\left(\varphi_{pm3} - \varphi_{b3}\right) \tag{3c}$$

TABLE 1 Specifications of the baseline machine.

Parameters	Symbol	Value
Machine rated power	P_{out}	1045 W
Winding turn number	N_t	60
PM volume	V_{pm}	27.2 cm^3
Stator outer radius	R_{os}	75 mm
Stator inner radius	R_{is}	40 mm
Rotor outer radius	R_{or}	39.5 mm
Rotor inner radius	R_{ir}	10 mm
Axial stack length	L_{stk}	100 mm
Air gap length	g	0.5 mm
Thickness of PM	h	2 mm
Saturated area flux density	B_{sat}	1.8 T
PM remanent flux density	b_r	1.2 T
Pole pitch	α	1
Magnet arc/pole pitch in barriers 1, 2, 3, 4	α_1, α_2, α_3, α_4	0.3, 0.52, 0.72, 0.91
Iron bridge width in barriers 1, 2, 3, 4	b_1, b_2, b_3, b_4	0.6 mm
Magnet width in barriers 1, 2, 3, 4	W_{pm1}, W_{pm2}, W_{pm3}, W_{pm4}	5, 7, 10, 12 mm

$$V_4 = R_4\left(\varphi_{pm4} - \varphi_{b4}\right) \tag{3d}$$

Solving the circuit model of Figure 5c, the PM flux in the air gap can be obtained as follows:

$$\varphi_{g1} = \frac{2V_1 + R_{g2}\varphi_{g2}}{2R_1 + R_{g1}} \tag{4a}$$

$$\varphi_{g2} = \frac{2V_2 + R_{g3}\varphi_{g3} - 2R_2\varphi_{g1}}{2R_2 + R_{g2}} \tag{4b}$$

$$\varphi_{g3} = \frac{2V_3 + R_{g4}\varphi_{g4} - 2R_3\varphi_{g1} - 2R_3\varphi_{g2}}{2R_3 + R_{g3}} \tag{4c}$$

$$\varphi_{g4} = \frac{2V_4 - 2R_4\varphi_{g1} - 2R_4\varphi_{g2} - 2R_4\varphi_{g3}}{2R_4 + R_{g4}} \tag{4d}$$

where φ_{g1}, φ_{g2}, φ_{g3}, φ_{g4} are the fluxes in the air gap that pass through the areas A_{g1}, A_{g2}, A_{g3}, A_{g4} respectively.

The circuit model of Figure 5c can accurately predict the PM flux profile in the air gap as shown in Figure 6a. However, as discussed in Section 2.3 in the proposed structure the reluctance of the air gap in each half of the magnetic pole is different. As a result, Figure 5c must be adjusted to accurately calculate the flux waveform in the proposed structure. The adjustment is done by replacing the air gap reluctance (R_g) with two unequal parallel reluctance elements as shown in Figure 7.

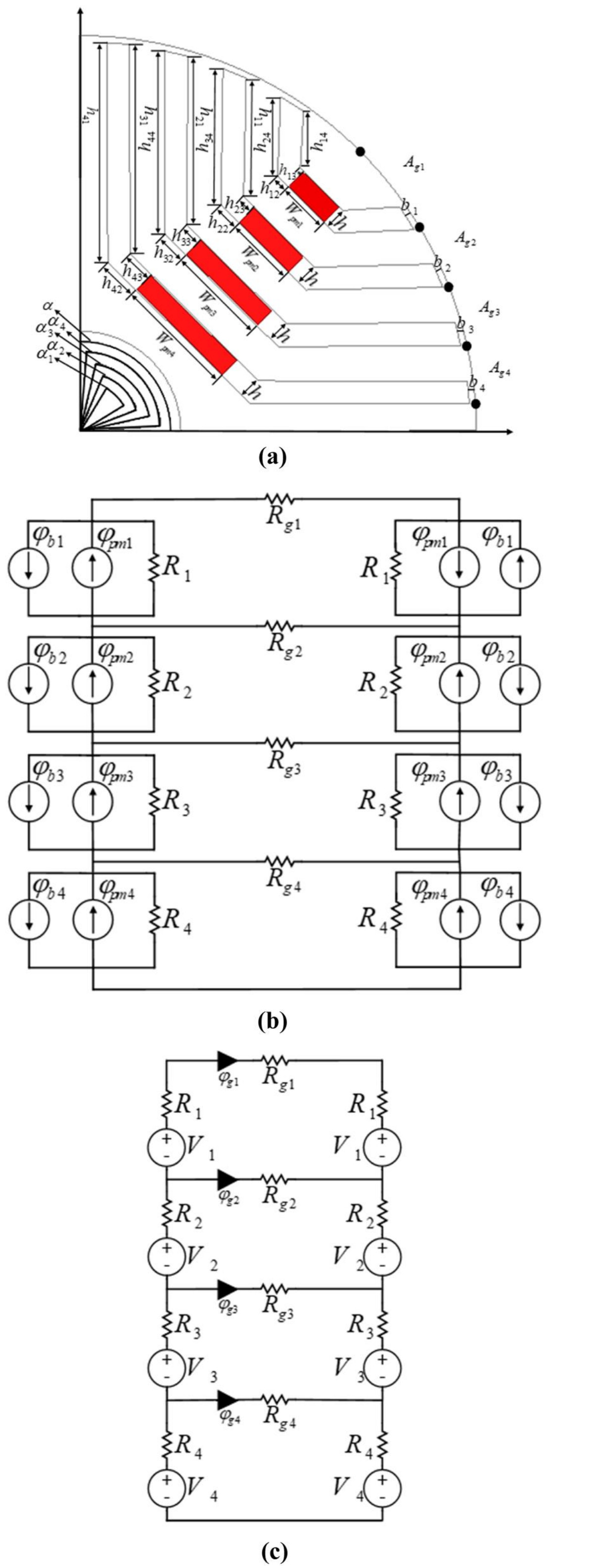

FIGURE 5 Magnetic circuit of a single pole (a) layout of a rotor pole (b) respective magnetic circuit model, and (c) simplified magnetic circuit model.

Using the adjusted circuit model the airgap flux distribution of the proposed structure is calculated and verified against FE in Figure 6b.

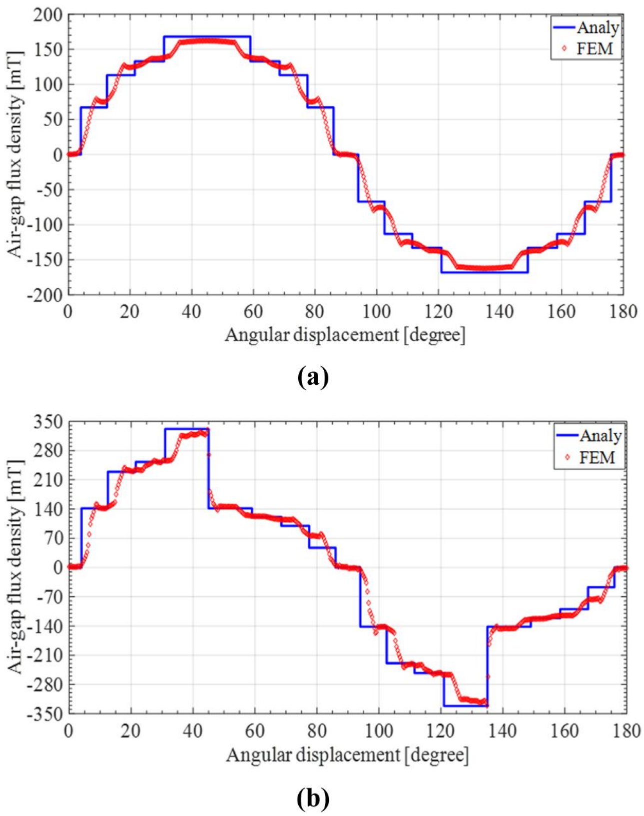

FIGURE 6 Distribution of Permanent Magnet (PM) flux in the air gap, (a) baseline machine. (b) Proposed machine (case study with ±2 mm).

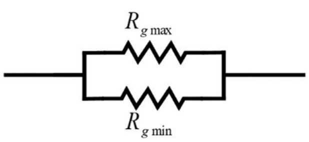

FIGURE 7 Circuit model representing the air gap reluctance in the proposed structure.

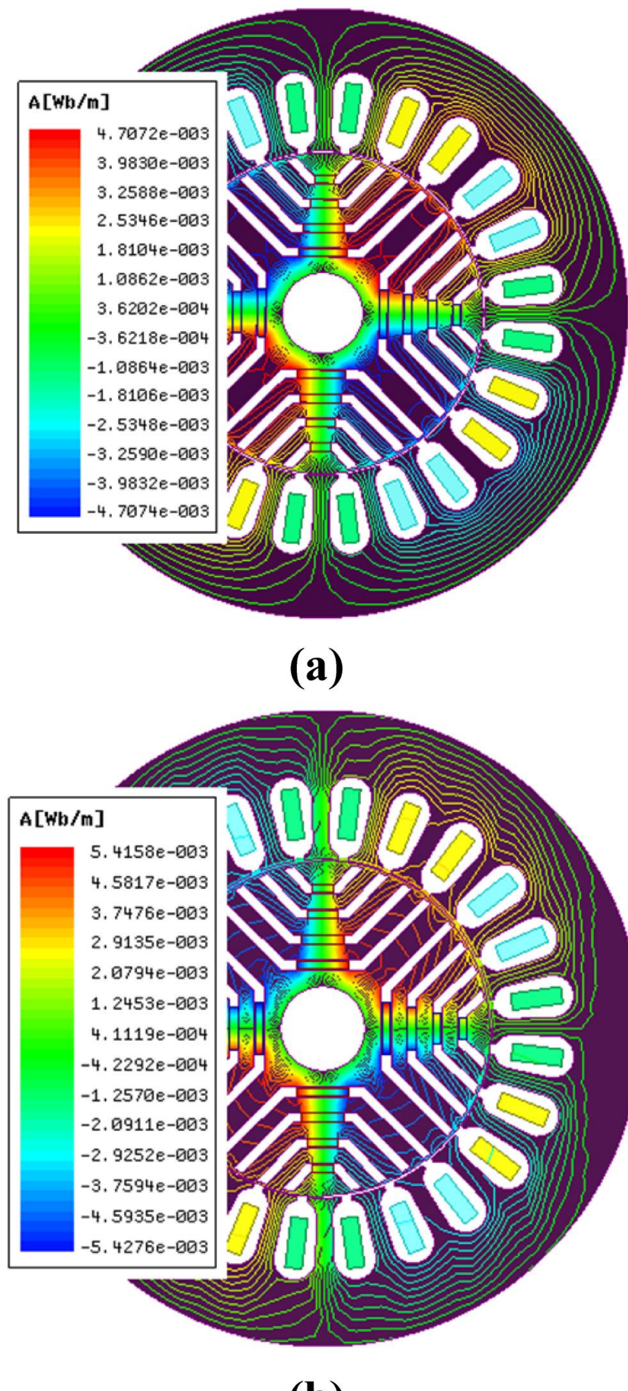

FIGURE 8 Distribution of magnetic flux lines at no-load operating condition, (a) baseline machine. (b) Proposed machine.

Figure 8 illustrates the distribution of magnetic flux lines and magnetic pole formation of both the reference (baseline) structure and the proposed structure under no-load operating condition. As expected, flux lines are slightly shifted to one side, and close their loop at a certain angle with respect to the baseline machine. This implies the rotor magnetic flux is shifted toward the q-axis consistent with the theory discussed in Section 2.2.

The back-EMF waveform of the proposed design is plotted and compared with the baseline structure in Figure 9. It is evident that the amplitude of the back-EMF voltage is increased despite the PM volume being the same as the baseline structure. This is because (1) magnetic flux is relatively concentrated and tilted toward one half of the pole, and (2) the reluctance of the flux path is decreased in half of the pole (sections where the core radii is extended or airgap is lowered). Since the generated PM flux is inversely proportional to the length of the airgap, the rate of change of PM flux in sections with the reduced airgap is higher than other sections. Therefore, the overall PM flux is strengthened and the back-EMF voltage is increased. This can also be justified by the circuit model of Figures 5 and 7. While the reluctance of the airgap in the baseline structure is R_g as shown in Figure 5, the reluctance of the airgap in the proposed structure is the equivalent parallel

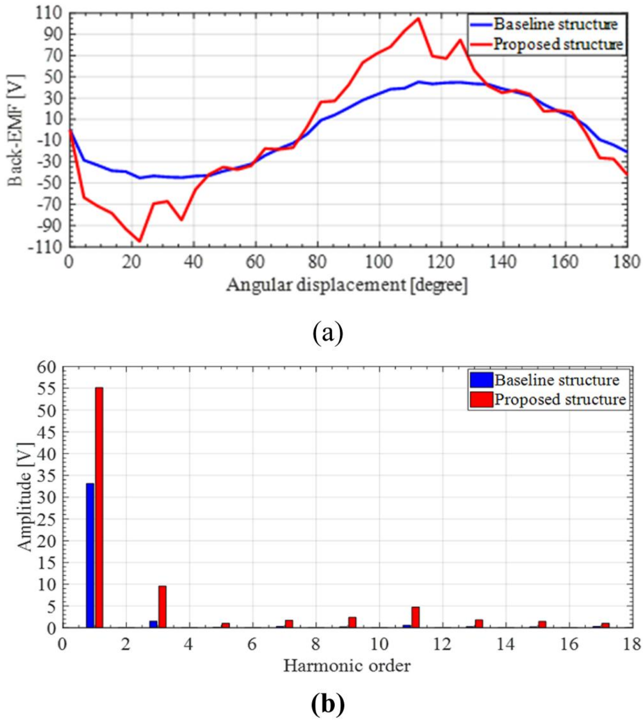

FIGURE 9 Back-EMF voltage, (a) waveform and (b) harmonic spectra.

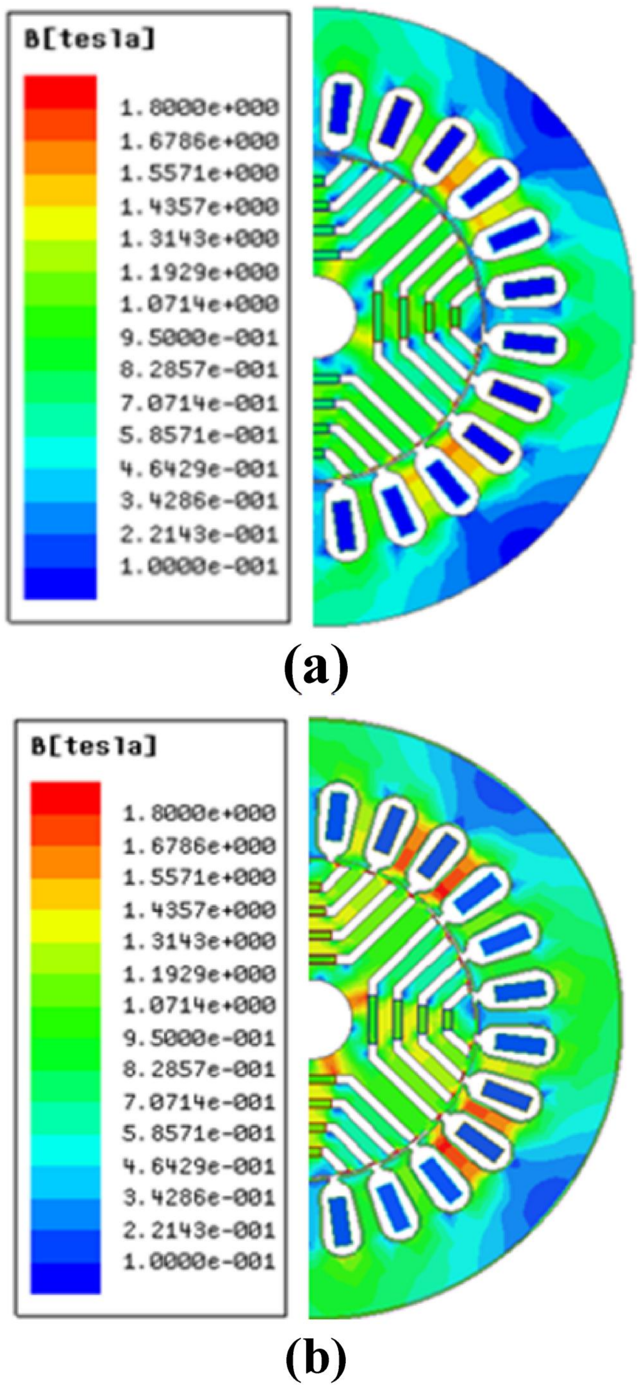

FIGURE 10 Magnetic flux density distribution at full load condition. (a) Baseline structure and (b) proposed structure.

of two reluctance elements as shown in Figure 7. As a result, in the proposed structure the reluctance of the airgap is less with respect to the baseline structure.

3.2 | Torque characteristic

Figure 10 presents the magnetic flux density distribution at the nominal load condition, indicating that the presented structure with uneven air gap length does not increase the saturation risk.

The FE-simulated resultant torque profile of both the proposed and the baseline structure is captured at full load condition and presented in Figures 11a and 12a, respectively. To capture these waveforms, the machine is driven and excited at low speed (e.g. 100 rpm) with rated DC current (i.e. $I_a = 5A$ $I_b = -2.5A$ $I_c = -2.5$ A), and the FE simulated resultant torque profile is recorded. It is evident that the proposed structure delivers a higher amount torque. Using Fourier transformation, the first and second components of the resultant torque (i.e. electromagnetic torque and reluctance torque respectively) are extracted and presented in Figures 11b and 12b. Since reluctance torque component oscillates as twice faster as the electromagnetic torque, the first torque harmonic is considered as electromagnetic torque and the second harmonic is considered as the reluctance torque.

As seen, the current phase angle corresponding to peak electromagnetic torque and peak reluctance torque are 45^o apart in baseline machine (Figure 11b). By contrast, since the rotor magnetic flux of the proposed structure is diverted toward the q-axis to a certain degree, the current angle corresponding to the peak torque components is reduced to 33.5 (Figure 12b). As a result, amplitude of the resultant torque exceeds the maximum torque delivery of the baseline machine. Note that the reluctance torque utility of the proposed structure is slightly higher compared to the baseline structure (i.e. 4.36 N.m vs. 4.1 N.m), confirming the theoretical discussion of Section 2.3.

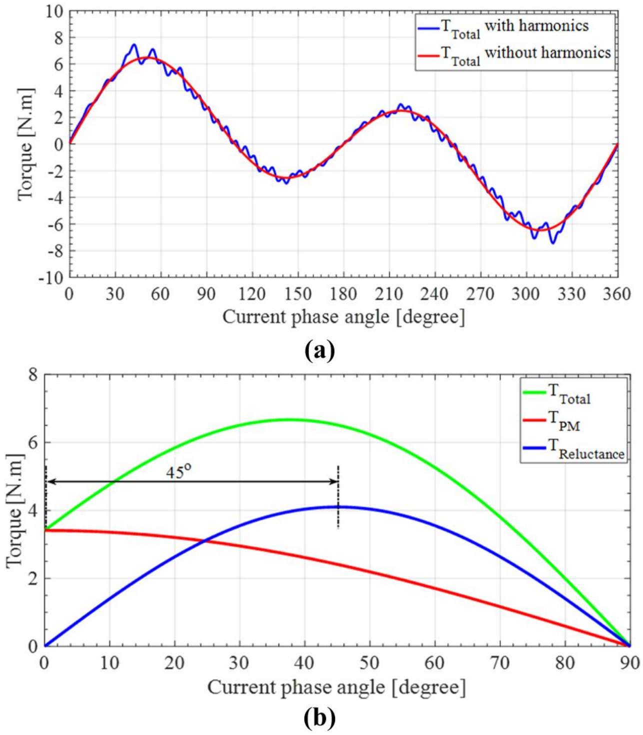

FIGURE 11 The profile of the output torque of the baseline structure (a) resultant torque and (b) individual torque components.

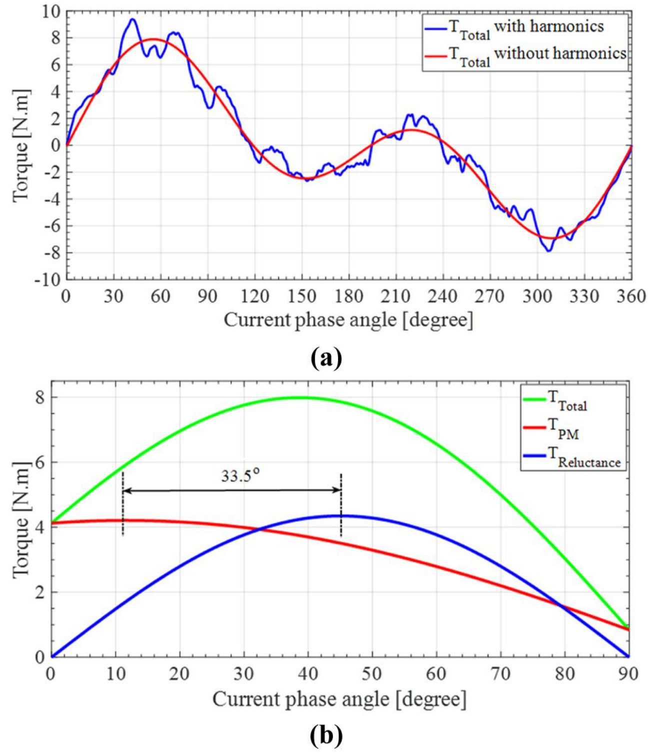

FIGURE 12 The profile of the output torque of the proposed structure (a) resultant torque and (b) individual torque components.

The instantaneous torque profile of the two structures when excited by ac current of 3.5 A (rms) and driven at rated speed of 1500 rpm is plotted in Figure 13. The average value of the instantaneous torque profile in Figure 13 is equal to the peak value of the resultant torque in Figure 12. The main operational setback of the proposed structure is that it could slightly magnify the torque ripple as implied in Figure 13, particularly because of the higher harmonic spectra of the back-EMF waveform (Figure 9b). Using Equation (5) as a metric for calculating the torque ripple [14], the ripple rises up from 19% in the baseline structure to 32% in the presented structure with uneven air gap of ±0.2 mm. This issue could be addressed by implementing various torque ripple mitigating measures available in the literature [21–25]. Possible solutions may include (i) reshaping of the magnets and/or the rotor frame, (ii) finding proper combination of slot and pole numbers, (iii) optimising the size/dimensions of magnets and also flux, and (iv) magnet skewing along the axial length.

$$T_{\text{Ripple}} = \frac{T_{\max} - T_{\min}}{T_{\text{avg}}} \tag{5}$$

Given that the rotor radii is shorten along one half of the magnetic pole and extended along the other half, this may result in unbalanced radial magnetic forces along the rotor circumference, generally known as unbalanced magnetic pull. To investigate this issue the total magnetic force exerted on the rotor during one rotation is simulated via FE and results are shown in Figure 14. As expected, the resultant magnetic

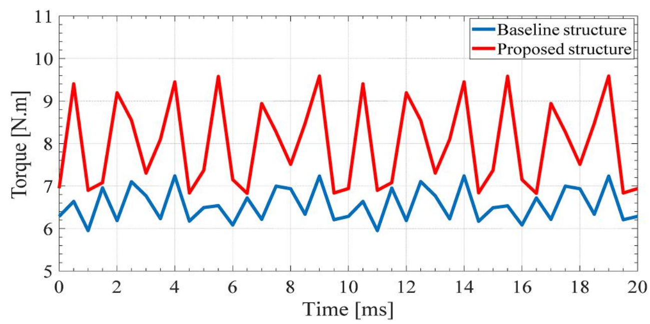

FIGURE 13 The instantaneous resultant torque profile.

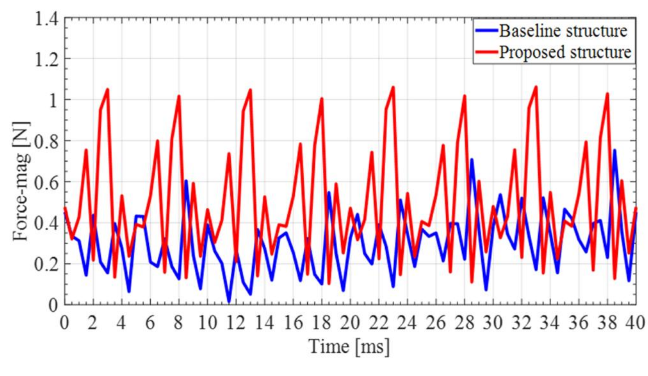

FIGURE 14 The total radial forces acting on the rotor during one rotation.

force acting on the proposed structure is relatively higher, but the total force is still less than 1 N and therefore, is not harmful to the motor. Although radial magnetic forces tend to increase locally in areas with lower air-gap size, these forces ultimately get cancelled out because of the structural symmetry of the rotor along the origin. Therefore, the resultant force remains below 1 N as confirmed by the FE simulation (Figure 14).

To identify to what extent the un-even air gap formation could impact the output torque delivery, sensitivity analysis is carried out for 5 different uneven air gap sizes, ranging from ±0.05 mm to ±0.25 mm as listed in Table 2. This range is selected based on mechanical and constructional limitation. The FE results indicate that the output torque delivery can rise up to 22.5% with respect to the baseline machine.

In Table 2, T_{Total}, T_{PM}, $T_{\mathrm{Reluctance}}$ are resultant torque, electromagnetic torque and reluctance torque, respectively, and angle τ represents the angular displacement of the current angle corresponding to the peak electromagnetic and the peak reluctance torque components. The index $\mathrm{T}^{+}_{\mathrm{Total}}$ % indicates the percentage of the resultant torque improvement with respect to the baseline structure.

To compare the torque production capability of the proposed structure versus the baseline machine with the same minimal air-gap, the baseline machine is simulated with different air-gap size(s), ranging from 0.5 to 0.25 mm (Table 3). Although minimal air-gap size(s) could result in slightly higher reluctance torque, the improvement of the electromagnetic torque is insignificant and still lower than the proposed structure. Also, because the peak reluctance torque and electromagnetic torque of the baseline machine are not aligned, the overall torque utility of the baseline machine (even in cases with minimal air-gap size(s)) is still below the proposed structure (Table 3).

TABLE 2 Output torque delivery per uneven airgap size.

	Baseline machine	Proposed machine				
Uneven air gap (mm)		0.05±	0.1±	0.15±	0.2±	0.25±
$T_{\mathrm{Reluctance}}$ (*N.m*)	4.1	4.2	4.27	4.28	4.35	4.36
T_{PM} (*N.m*)	3.41	3.95	4.05	4.1	4.21	4.28
τ (degrees)	45	39	37.5	35.9	33.5	30.5
T_{Total} (*N.m*)	6.66	7.42	7.63	7.74	8	8.16
$\mathrm{T}^{+}_{\mathrm{Total}}$ %		11.4	14.5	16.2	20.1	22.5

TABLE 3 Output torque delivery for different air gap sizes.

	Baseline structure						Proposed structure
Air gap sizes (mm)	0. 5	0.45	0.4	0.35	0.3	0.25	0.5 ± 0.25
$T_{\mathrm{Reluctance}}$ (*N.m*)	4.1	4.3	4.45	4.63	4.8	4.96	4.36
T_{PM} (*N.m*)	3.41	3.42	3.45	3.47	3.48	3.5	4.28
τ (degrees)	45	45	45	45	45	45	30.5
T_{Total} (*N.m*)	6.66	6.87	7	7.22	7.4	7.57	8.16

3.3 | Power factor

To calculate the power factor, the armature winding is excited by a balanced 3-phase sinusoidal current source of 3.5 A rms (5 A max) and the voltage induced across the internal terminal of the phase winding is recorded. The input voltage profile is captured by adding the resistive voltage drop to the back-EMF waveform. The power factor of the machine is calculated based on the phase shift between the fundamental input voltage and the sinusoidal input phase current as marked in Figure 15. Since the amplitude of the input voltage is much higher (in the order of 200 V), and for a better visibility the excitation current is scaled up (multiplied by 30), but the current unit is defined as (A/30). The waveforms and data presented in Figures 13 and 15 are related to the case study with the uneven air gap of ±0.2 mm. The basic steady state performance characteristics of the machine are compared with the baseline structure and summarised in Table 4. As presented in Table 4, the proposed structure operates at a higher power factor (with respect to the baseline structure) because of relatively higher amplitude of the back-EMF voltage (Figure 9). Therefore, in addition to aligning/synching the two torque components, the proposed arrangement increases the flux level and the back-EMF, and thereby allows the machine to operate at a higher power factor.

4 | EXPERIMENTAL VALIDATION

For verification purposes, the prototype of the proposed structure with uneven air gap of ±0.2 mm is built and tested. The rotor magnets are inserted inside 4 layers of flux barriers at their centre. The PM width varies per layer trending from 12 mm at the inner layer next to the rotor shaft to 10 mm, 7 and 5 mm toward the outer layers. The PM thickness and the axial length are fixed and identical in every layer (i.e. 2 mm

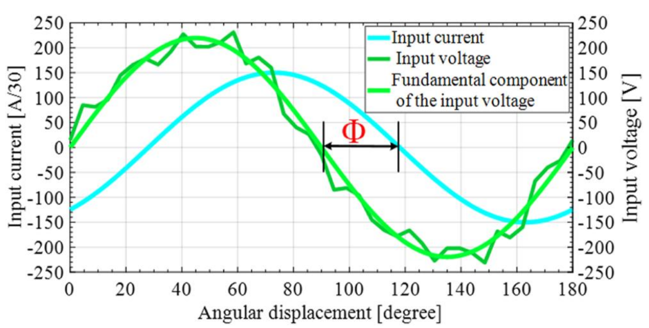

FIGURE 15 Power factor calculation.

TABLE 4 Basic steady state performance characteristic.

	Baseline machine	Proposed machine				
Uneven air gap (mm)		0.05±	0.1±	0.15±	0.2±	0.25±
Back-EMF RMS (V)	33.12	51.74	52.38	53	55.13	56.6
Output power (W)	1045	1148	1176	1189	1221	1242
Total loss (W)	255	250	237.6	237.9	225	218
Power factor	0.822	0.879	0.881	0.881	0.882	0.883
Efficiency (%)	80.38	82.11	83.19	83.32	84.44	84.94

thickness along radial direction and 20 mm length along axial direction). Because a 12 mm width PM was not available in the market, the inner/bottom layer is filled with two rows of PMs with the width of 7 and 5 mm to form a PM with the target width of 12 mm. The prototyped model and the test rig are shown in Figure 16.

The profile of the back-EMF waveform is measured and compared with the one previously obtained from FE simulation (Figure 17). To capture the maximum output torque, the motor is driven at low speed (e.g. 100 rpm) and stator winding is excited by the rated DC current (i.e. $I_a = 5$A, $I_b = -2.5$ A, $I_c = -2.5$ A) and the static torque is measured at different rotor positions (Figures 17 and 18). The torque value at a particular rotor position is essentially the maximum torque at the corresponding rotor position. The maximum torque recorded during the measurement phase was 7.88 N.m which is fairly close to the simulated value of 8 N.m.

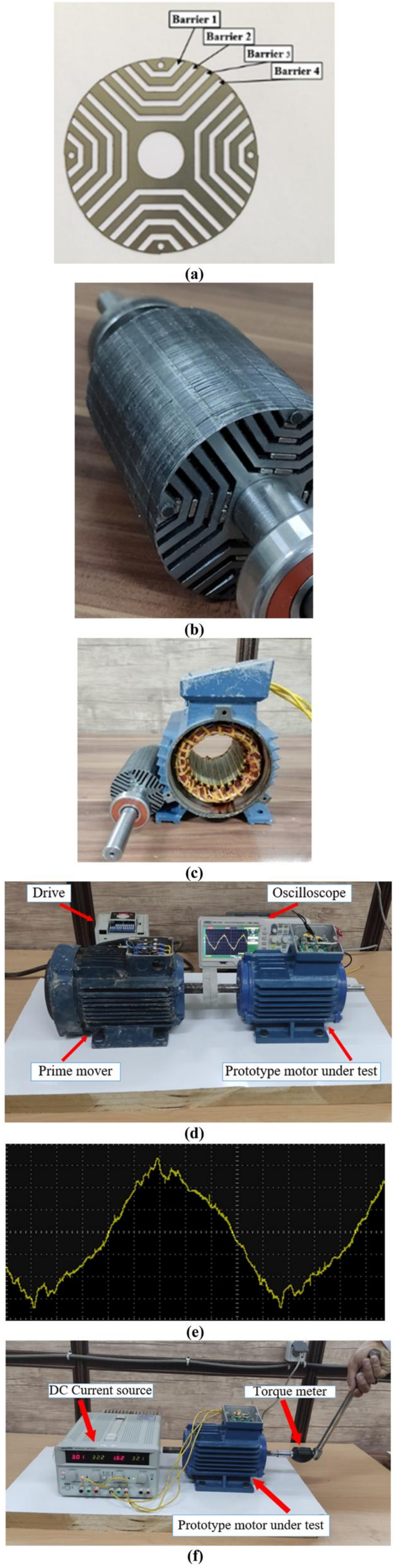

FIGURE 16 Prototyped machine, (a) rotor sheet, (b) rotor assembly, (c) rotor and stator assembly, (d) test rig under generating mode, (e) measured phase back EMF, and (f) test rig under motoring mode.

5 | CONCLUSION

A new design of PM-Assisted SynRM with shifted magnetic poles was introduced to enhance the electromagnetic torque and maximise the resultant torque (i.e. reluctance torque plus electromagnetic torque) utility by synching the torque components near a same current phase angle. The magnetic pole shifting came to fruition by forming uneven air gap along the magnetic pole arc angle without altering the structural arrangement of magnets and flux barriers. Therefore, the mechanical stiffness of the machine remain intact. In addition to the saliency created by the flux barriers, the uneven air-gap further increases the saliency ratio $(\frac{L_d}{L_q})$, and therefore boosts the reluctance torque utility. Furthermore, the presented pole shifting scheme is not exclusive to a particular type of PM-Assisted SynRM but can be applied to a wide variety type of PM-Assisted SynRMs. To determine the level success, the electromagnetic performance of the proposed design was compared against the baseline structure under the same operating condition. For further verification, the functionality of the machine was verified through a series of experimental tests.

It is noted that the proposed uneven air gap structure could slightly increase the torque ripple which is considered as the main operation setback of the proposed scheme. The future research on this topic may include optimising the structural parameters of the machine, and investigating counter-measures to nullify the added torque ripple and vibration analysis.

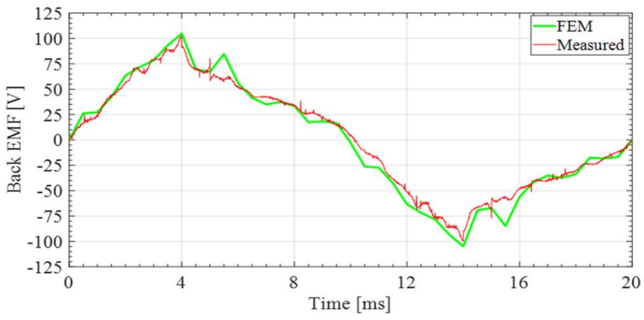

FIGURE 17 The finite element (FE) simulated and measured back EMF waveform.

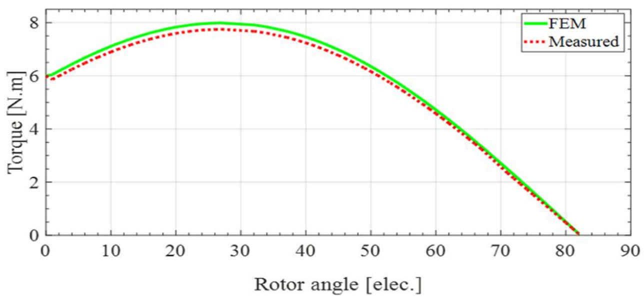

FIGURE 18 The finite element (FE) simulated and measured of the resultant torque profile.

AUTHOR CONTRIBUTION

Seyyed Morteza Mousavi Bafrouei: Conceptualization (lead); data curation (lead); formal analysis (lead); investigation (lead); methodology (lead); project administration (supporting); resources (supporting); software (lead); supervision (supporting); validation (lead); visualization (lead); writing-original draft (lead); writing – review and editing (lead). **Aliakbar Damaki Aliabad**: Conceptualization (lead); data curation (supporting); formal analysis (lead); investigation (lead); methodology (lead); project administration (lead); resources (lead); software (supporting); supervision (lead); validation (lead); visualization (supporting); writing-original draft (supporting); writing – review and editing (lead). **Ebrahim Amiri**: Conceptualization (supporting); data curation (supporting); formal analysis (lead); investigation (lead); methodology (lead); project administration (supporting); resources (supporting); software (supporting); supervision (supporting); validation (supporting); visualization (supporting); writing-original draft (lead); writing – review and editing (lead).

ACKNOWLEDGEMENTS

No funding information.

CONFLICT OF INTEREST STATEMENT

No conflict of interest.

DATA AVAILABILITY STATEMENT

Data sharing not applicable to this article as no datasets were generated or analysed during the current study.

ORCID

Seyyed Morteza Mousavi Bafrouei https://orcid.org/0000-0001-7818-0054

REFERENCES

1. Cai, H., Guan, B., Xu, L.: Low-cost ferrite PM-assisted synchronous reluctance machine for electric vehicles. IEEE Trans. Ind. Electron. 61(10), 5741–5748 (2014). https://doi.org/10.1109/tie.2014.2304702
2. Hu, R., et al.: Design and sensitivity analysis of a high performance ferrite PM-assisted synchronous reluctance motor for water pump applications. In: 2021 24th International Conference on Electrical Machines and Systems (ICEMS), Gyeongju. Korea (2021). https://doi.org/10.23919/ICEMS52562.2021.9634598
3. Gowtham, V., Sashidhar, S.: Hybrid ferrite Al-Ni-Co PM assisted synchronous reluctance motor for air-conditioner compressors. In: IECON 2021 – 47th Annual Conference of the IEEE Industrial Electronics Society. Toronto (2021). https://doi.org/10.1109/IECON48115.2021.9589289
4. Parasiliti, F., et al.: Finite-Element-based multiobjective design optimization procedure of interior permanent magnet synchronous motors for wide constant-power region operation. IEEE Trans. Ind. Electron. 59(6), 2503–2514 (2012). https://doi.org/10.1109/tie.2011.2171174
5. Ma, Q., Refaie, A.E.: Finite element-based multi-objective design optimization of IPM considering saturation effects for constant power region of operation. In: 2020 IEEE Energy Conversion Congress and Exposition (ECCE). Detroit (2020). https://doi.org/10.1109/ECCE44975.2020.9236049
6. Zhao, W., et al.: A new hybrid permanent magnet synchronous reluctance machine with axially sandwiched magnets for performance improvement. In: 2022 IEEE Transactions on Energy Conversion, vol. 33, pp. 2018–2029 (2018)
7. Cheng, Y., et al.: Sensitivity analysis and multi-objective optimization of a PM-assisted synchronous reluctance motor with rectangular flux-barriers. In: 2021 IEEE 4th Student Conference on Electric Machines and Systems (SCEMS). Huzhou, China (2021). https://doi.org/10.1109/SCEMS52239.2021.9646098
8. Grundmann, D., et al.: Design and optimization of a quadruple 3-phase permanent magnet assisted synchronous reluctance machine. In: IECON 2021 – 47th Annual Conference of the IEEE Industrial Electronics Society. Toronto (2021). https://doi.org/10.1109/IECON48115.2021.9589798
9. Wu, W., et al.: Design and analysis of a hybrid permanent magnet assisted synchronous reluctance motor considering magnetic saliency and PM usage. IEEE Trans. Appl. Supercond. 28(3), 1–6 (2018). https://doi.org/10.1109/tasc.2017.2775584
10. Gowtham, V., Sashidhar, S.: Comparison of hybrid PM assisted synchronous reluctance motors. In: 2021 22nd IEEE International Conference on Industrial Technology (ICIT). (2021). https://doi.org/10.1109/ICIT46573.2021.9453679
11. Zhao, W., et al.: Design and analysis of a novel PM-assisted synchronous reluctance machine with axially integrated magnets by the finite-element method. IEEE Trans. Magn. 53(6), 1–4 (2017). https://doi.org/10.1109/tmag.2017.2662717
12. Nobahari, A., Vahedi, A., Zarandi, R.N.: A modified permanent magnet-assisted synchronous reluctance motor design for torque characteristics improvement. IEEE Trans. Energy Convers. 37(2), 989–998 (2022). https://doi.org/10.1109/tec.2021.3127081
13. Zhao, W., et al.: Performance improvement of ferrite-assisted synchronous reluctance machines using asymmetrical rotor configurations. IEEE Trans. Magn. 51(11), 1–4 (2015). https://doi.org/10.1109/tmag.2015.2436414
14. Zhao, W., et al.: Optimal design of a novel V-type interior permanent magnet motor with assisted barriers for the improvement of torque characteristics. IEEE Trans. Magn. 50, 11–14 (2014). https://doi.org/10.1109/tmag.2014.2330339
15. Mohammadi, A., Mirimani, S.M.: Design of a novel PM-assisted synchronous reluctance motor topology using V-shape permanent magnets

for improvement of torque characteristic. IEEE Trans. Energy Convers. 37(1), 424–432 (2022). https://doi.org/10.1109/tec.2021.3109079
16. Bianchi, N., Mahmoud, H., Bolognani, S.: Fast synthesis of permanent magnet assisted synchronous reluctance motors. IET Electr. Power Appl. 10(5), 312–318 (2016). https://doi.org/10.1049/iet-epa.2015.0240
17. Ngo, D.K., Hsieh, M.-F.: Performance analysis of synchronous reluctance motor with limited amount of permanent magnet. Energies 12(18), 3504 (2019). https://doi.org/10.3390/en12183504
18. Poudel, B., et al.: Toward less rare-earth permanent magnet in electric machines: a review. IEEE Trans. Magn. 57(9), 1–19 (2021). https://doi.org/10.1109/tmag.2021.3095615
19. Deng, X., et al.: Design and finite element analysis of a novel permanent magnet assisted reluctance synchronous motor. Appl. Comput. Electromagn. Soc. J. 35(9), 1012–1021 (2020). https://doi.org/10.47037/2020.aces.j.350906
20. Ghahfarokhi, M.M., et al.: Computationally efficient analytical model of interior permanent magnet machines considering stator slotting effects. IEEE Trans. Ind. Appl. 58(4), 4587–4601 (2022). https://doi.org/10.1109/tia.2022.3170536
21. Liu, H., et al.: Design of permanent magnet-assisted synchronous reluctance motor for maximized back-EMF and torque ripple reduction. IEEE Trans. Magn. 53(6), 1–4 (2017). https://doi.org/10.1109/tmag.2017.2663319
22. Sudheer, S., et al.: Optimal torque ripple reduction technique for outer rotor permanent magnet synchronous reluctance motors. IEEE Trans. Energy Convers. 33(3), 1184–1192 (2018). https://doi.org/10.1109/tec.2017.2781259
23. Bianchi, N., Bolognani, S.: Design techniques for reducing the cogging torque in surface mounted PM motors. IEEE Trans. Ind. Appl. 38(5), 1259–1265 (2002). https://doi.org/10.1109/tia.2002.802989
24. Song, J., et al.: Optimal design of permanent magnet linear synchronous motors based on Taguchi method. IET Electr. Power Appl. 11(1), 41–48 (2017). https://doi.org/10.1049/iet-epa.2016.0164
25. ZhaoLipo, W.T.A., Kwon, B.: Torque pulsation minimization in spoke-type interior permanent magnet motors with skewing and sinusoidal permanent magnet configurations. IEEE Trans. Magn. 51(11), 1–4 (2015). https://doi.org/10.1109/tmag.2015.2442977

How to cite this article: Mousavi Bafrouei, S.M., Aliabad, A.D., Amiri, E.: Design and analysis of PM-assisted synchronous reluctance machine with shifted magnetic poles. IET Electr. Power Appl. 18(1), 52–63 (2024). https://doi.org/10.1049/elp2.12366